Available online at www.sciencedirect.com
ScienceDirect
Engineering Fracture Mechanics xxx (2007) xxx–xxx
Engineering Fracture Mechanics
www.elsevier.com/locate/engfracmech

A numerical study of inclusion–matrix debonding in the presence of a nearby crack

P.C. Savalia, H.V. Tippur *, M.S. Kirugulige

Department of Mechanical Engineering, Auburn University, Auburn, AL 36849, USA

Received 5 February 2007; received in revised form 8 May 2007; accepted 10 May 2007

Abstract

Debonding of an inclusion from the surrounding matrix in the presence of a nearby crack tip is studied numerically. Finite element models of symmetric three-point bend configurations are implemented in conjunction with a stiffness degradation method and the maximum tensile stress criteria to investigate the influence of debonding on crack tip parameters. The geometry considered is a single edge cracked beam having a symmetrically positioned stiff or soft cylindrical inclusion ahead of the crack tip. The numerical model is first validated by interferometric measurements on an edge cracked epoxy specimen with a glass inclusion. The measured quantities namely, the crack mouth opening displacement, crack mouth compliance, energy release rate, dominant strain, are all successfully captured by the adopted numerical methodology, before and after the inclusion debonds from the matrix. Subsequently, the effects of parameters such as the distance between the crack tip and inclusion center (L), the inclusion diameter (d), and the Young's modulus ratio between the inclusion and the matrix, are studied using the model. A stiff inclusion of constant (d/L) ratio debonds from the matrix at higher load levels when the inclusion interface is farther away from the crack tip. The increase in the crack driving force due to debonding is the highest when the inclusion proximity parameter ρ is approximately 0.4 and it decreases when ρ is increased or decreased relative to this value. However, when d/L ratio is varied, higher crack driving forces due to debonding are observed for larger size inclusions due to a greater loss of crack tip shielding and reinforcement. The influence of the modulus ratio (E_i/E_m) due to debonding is most prominent in the range 0–1 for fixed d/L and ρ values. Additionally, a stiffer inclusion tends to debond from the matrix at lower loads for a constant interfacial strength.

Keywords: Energy release rate; Crack opening displacements; Interfacial debonding; Crack–inclusion interactions; Finite element method; Optical interferometry

1. Introduction

Failure processes in multiphase materials such as fiber reinforced composites, particulate composites, functionally graded materials and syntactic foams are strongly linked to the basic problem of a matrix crack

* Corresponding author.
E-mail address: tippuhv@auburn.edu (H.V. Tippur).

0013-7944/$ - see front matter © 2007 Elsevier Ltd. All rights reserved.
doi:10.1016/j.engfracmech.2007.05.012

interacting with a second phase inclusion. A perfect bond seldom exists between a matrix and a second phase reinforcement. As a result interfacial debonding between the two is a common occurrence which in turn affects the overall failure behavior. This issue has motivated several continuum mechanics based analyses of a stationary elastic crack interacting with an inclusion. Using complex potentials, Tamate [1] addressed interaction between a matrix crack and a circular inclusion in uniaxially loaded planar sheets. A lowering of crack tip stress intensity when the inclusion is stiff and the opposite when it is compliant relative to the matrix is demonstrated. The effect of the distance between the crack tip and the inclusion is studied in a work by Atkinson [2] under uniaxial and biaxial loading conditions. He has reported stress intensity factors as a function of crack lengths and elastic properties of the inclusion. Using Green's functions Erdogan et al. [3] also studied matrix crack–inclusion interactions. The interaction between a crack and a hole or an inclusion in tensile sheets and the resulting critical values of applied stress for crack extension and crack extension angles are reported by Gdoutos [4,5]. Hasebe et al. [6] examined stress fields near a debond tip in a tensile configuration by modeling crack–inclusion interaction as a mixed boundary value problem. The role of the shape of an inclusion and its orientation relative to a crack tip are studied by Patton and Santare [7] by considering an elliptical inclusion ahead of a crack tip in a planar medium. A reduction in the crack tip stress intensity as the tip orients towards the broader side of the inclusion is demonstrated. The effects of inclusion translation, rotation and expansion relative to the crack tip on energy release rate are studied by Li and Chudnovsky [8,9]. A crack is shown to accelerate as it approaches a soft inclusion while the opposite occurs for a stiff inclusion.

A few numerical studies of the problem are also reported in the literature. Most works to date use boundary element formulations. A matrix crack interacting with an inclusion is modeled by Bush [10] to study crack paths and the associated energy release rates at initiation and growth. The stress shielding and amplification effects are shown to occur as the crack tip approaches and recedes from the inclusion, respectively. He also modeled the effect of a weak interface between an inclusion and a matrix by introducing a debond along the inclusion periphery. An increase in the energy release rate and crack attraction towards the inclusion–matrix interface is shown. Alternatively, Knight et al. [11] studied the problem by introducing an interphase region around an inclusion to investigate the effect of Poisson's ratio. They observe that as the Poisson's ratio of the matrix phase approaches the incompressibility limit, both shielding effects and crack deflections reduce. The thickness of the interphase region is shown to affect the crack growth behavior depending on the relative mismatch in properties between the matrix, inclusion and interphase. A boundary element based on symmetric Galerkin formulation is implemented by Kitey et al. [12] to study crack growth behavior in the presence of an isolated inclusion or a cluster of inclusions. They note that cluster orientation produces different crack paths but the overall energy dissipation remains unchanged.

The works cited above examine the role of a well bonded inclusion or a debonded inclusion on crack tip parameters. However, the evolution of debonding of an inclusion and the resulting effect on crack tip parameters remains unexplored and is undertaken in the current study using finite element simulations. A stiffness degradation approach is adopted to explore the effects of inclusion size, inclusion proximity to the crack tip and the Young's modulus mismatch between the inclusion and matrix on fracture parameters, before and after debonding. The methodology is first verified using independent measurements from optical interferometry on a benchmark example. Subsequently, the method is used to study different parameters of interest.

2. The approach

The finite element method is used to study the evolution of inclusion–matrix debonding process in the presence of a nearby crack tip. The approach involves deactivating the stiffness of a layer of elements surrounding an inclusion when a specified failure criterion is met.[1] A few previous works have successfully adopted such a methodology to simulate initiation and progression of failure in materials. Al-Ostaz and Jasiuk [16] simulated

[1] Cohesive element formulations [13] have become popular in recent years for numerically simulating formation of new surfaces in materials. Several investigators have developed and/or adopted this approach for interfacial failure simulations under static and dynamic loading conditions [14,15]. If one were to utilize the cohesive elements approach, however, interfacial fracture parameters such as the fracture energy and critical normal separation distance for the inclusion–matrix system would be necessary. Accordingly, the element stiffness deactivation method is used in this work due to its relative simplicity.

Please cite this article in press as: Savalia PC et al., A numerical study of inclusion–matrix debonding in the ..., Eng Fract Mech (2007), doi:10.1016/j.engfracmech.2007.05.012

crack growth in porous materials under uniaxial tension. They investigated crack trajectories in perforated epoxy sheets by considering the elastic strain energy and maximum in-plane principal stress based failure criteria for simulating progressive failure. Ko et al. [17] also used this method to simulate fracture in a punch problem dominated by shear failure with a ductile-fracture criterion based on effective strain. They show that an improved solution is possible if the fracture strain of the material is determined experimentally and used as an input in the numerical model.

3. Model description

A finite element model was developed in ANSYS™ [18] structural analysis environment for studying crack–inclusion interaction in terms of geometrical and material parameters. APDL (ANSYS Parametric Design Language) macros were developed for constructing and solving the model and for post-processing results. A symmetric three-point bend geometry (152 mm × 42.5 mm × 7.1 mm) was created by specifying key-points, linking them by lines and creating areas in a 2D space. A symmetrically located sharp edge crack was modeled from unmerged areas having common sides forming the two crack faces. Isoparametric quadrilateral elements (PLANE 82 in ANSYS™ [18]) with mid-side nodes were used to generate a controlled mesh for the whole model. The analysis was performed under plane stress assumptions. A representative finite element mesh used in these simulations is shown in Fig. 1a. It also shows an enlarged view of the discretization in the vicinity of the crack tip-inclusion pair. A fine mesh (with an element size of nearly $a/200$, where a is the crack length) was used in regions of interest namely, near the crack tip and around the inclusion, to capture steep gradients in various mechanical fields. The model contained roughly 7356 elements and 22,323 nodes. A set of elements forming the interface between the inclusion and matrix was generated, as shown in Fig. 1a, to have a thickness of $\sim d/100$ (and was guided by experimental observations, to be discussed later on), d being the inclusion diameter. The geometrical parameters and the coordinate systems associated with the model are shown schematically in Fig. 1b. In addition to the crack tip coordinate system with its origin at O, another with origin O'

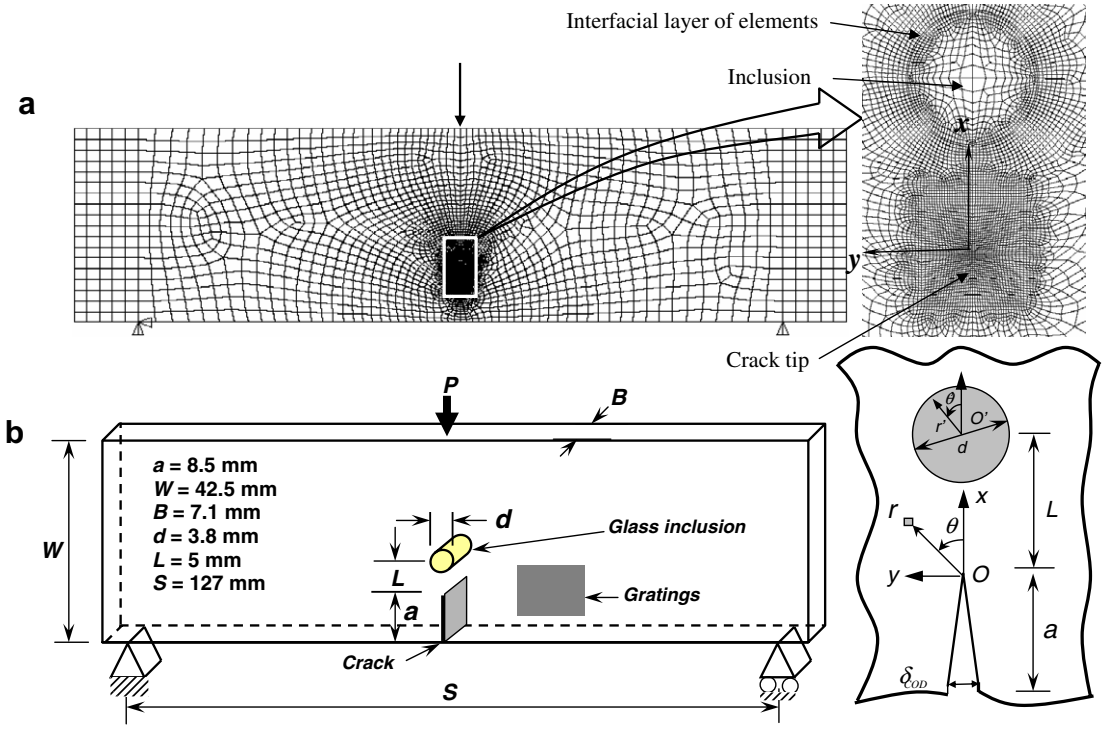

Fig. 1. (a) Finite element mesh used for simulating crack–inclusion interactions and inclusion debonding. (b) Specimen details: specimen geometry and loading configuration, crack tip and inclusion coordinate systems.

Please cite this article in press as: Savalia PC et al., A numerical study of inclusion–matrix debonding in the ..., Eng Fract Mech (2007), doi:10.1016/j.engfracmech.2007.05.012

Table 1
Elastic properties of matrix and inclusion

	Young's modulus E (GPa)	Poisson's ratio ν
Epoxy	3.5	0.35
Glass	68	0.19

at the center of the inclusion was also considered. In Fig. 1b, L is the distance between the crack tip and the center of the inclusion, d is the inclusion diameter and a is the crack length.

An inclusion–matrix pair consisting of glass–epoxy as test materials was first modeled. (The elastic properties of glass and epoxy are listed in Table 1.) The choice of the material system allowed a direct validation of the model by experiments. A criteria based on the strength of glass–epoxy interface was hypothesized to simulate debonding of the inclusion from the matrix. The aforementioned interfacial elements constituting the bond layer were useful for this purpose. The radial stress (relative to the origin O' in Fig. 1b) was used for debonding the inclusion–matrix interface. It was hypothesized that debonding occurs when the radial stress reaches the interfacial strength in these elements. A concentrated force (P) was imposed symmetrically on the model in small increments to achieve mode-I conditions. During the loading phase, elements in the bonding layer were monitored for radial stress. The computed data was post-processed at the end of each load step. When a predefined value of positive radial stress was attained in the bond layer, the corresponding elements were 'killed' (deactivated) using the so-called 'element death' (EKILL) option available in ANSYS. This was accomplished by a means of a user-defined subroutine. It should be noted that the desired effect was achieved by not actually removing the 'killed' elements from the model but by multiplying their stiffness by a severe reduction factor. (In this work a reduction factor of 1×10^{-8} was used.) This prevents those deactivated elements from contributing to the overall stiffness of the structure in the subsequent loading steps. That is, the respective rows and columns of the stiffness matrix were made negligibly small without replacing them by zeros. Respective loads in the load vector were also zeroed out but not removed from the vector. Deactivating an element in the model can cause large rigid body displacements (especially rotations) in the neighboring elements. This could give rise to spurious strains. In order to overcome this, large rotation effects were included.[2] This option separates the rigid rotations from the total deformation and uses appropriate updating procedure for rotations to take care of incremental objectivity.

As mentioned earlier, the criteria used for deactivating an element in the bond layer can be expressed as

$$\sigma_{rr} = (\sigma_{int})_{cr}, \tag{1}$$

where $(\sigma_{int})_{cr}$ is the interfacial strength in tension and σ_{rr} is the radial stress relative to the origin O'. The interfacial strength of a glass–epoxy pair was measured experimentally in an earlier study [19] and was 9.25 ± 1.7 MPa.

The variation of σ_{rr} around the inclusion is shown in Fig. 2. As expected σ_{rr} around is continuous before the onset of debonding and is maximum on the interfacial location directly ahead of the crack tip ($\theta = 0°$, $\theta' = 180°$). Once debonding occurs, σ_{rr} vanishes over the debonded interface. That is, debonding occurs between $\theta' = -180°$ to 0° and 110° to 180° as shown in Fig. 2. The asymmetry in debonding is due to a crack path selection that occurs due to one fixed and one roller boundary condition used at the left and right supports, respectively. (This also helps to mimic the experimental asymmetries, to be discussed later on, as well.)

A plot of the crack mouth opening displacement (CMOD) as a function of the applied load for the above case is shown in Fig. 3a. The plot shows a linear variation of CMOD with load until the onset of debonding. The post-debonding regime has a noticeably different slope with a transition zone clearly visible in the plot. This difference is brought out prominently by evaluating the crack mouth compliance, identified in this work as the rate of change of CMOD with respect to the imposed load P (=d(CMOD)/dP). This is obtained by differentiating CMOD data using a central difference scheme and the result is shown in Fig. 3b as a solid line.

The crack opening displacements along the crack face (r, $\theta = 180°$) were extracted to determine mode-I stress intensity factors (K_I) as a function of the applied load. The method of displacement regression was used

[2] Subroutine NLGEOM, ON in ANSYS.

Please cite this article in press as: Savalia PC et al., A numerical study of inclusion–matrix debonding in the ..., Eng Fract Mech (2007), doi:10.1016/j.engfracmech.2007.05.012

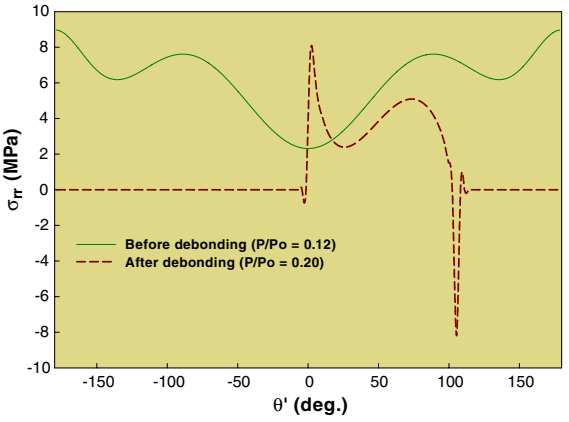

Fig. 2. Radial stress distribution around the inclusion before and after debonding of the inclusion from the matrix.

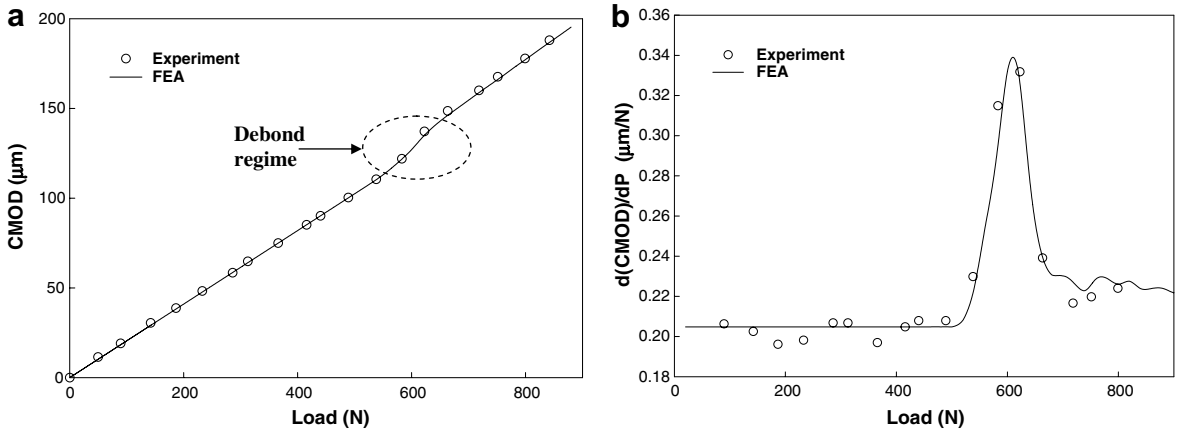

Fig. 3. Comparison of experimentally obtained CMOD variations for crack–inclusion specimen: (a) variation of CMOD with load and (b) variation of crack mouth compliance with load.

for evaluating K_I. Using Williams' asymptotic expansion, the apparent stress intensity factor $(K_I)_{app}$ at different crack face locations can be expressed as [20]

$$(K_I)_{app} \approx K_I + Cr, \tag{2}$$

where

$$(K_I)_{app} = \frac{E\delta\sqrt{2\pi}}{4\sqrt{r}} \tag{3}$$

and E is the Young's modulus, δ is the crack opening displacement at a radial distance r measured from the crack-tip and C is the coefficient of the higher order term in the expansion. Based on Eq. (3), by plotting $(K_I)_{app}$ as a function of r, one can perform linear regression of $(K_I)_{app}$ values to find K_I as

$$K_I = \lim_{r\to 0}(K_I)_{app}. \tag{4}$$

Using the K_I value, the corresponding energy release rate G can then be determined as

$$G = \frac{K_I^2}{E}. \tag{5}$$

Please cite this article in press as: Savalia PC et al., A numerical study of inclusion–matrix debonding in the ..., Eng Fract Mech (2007), doi:10.1016/j.engfracmech.2007.05.012

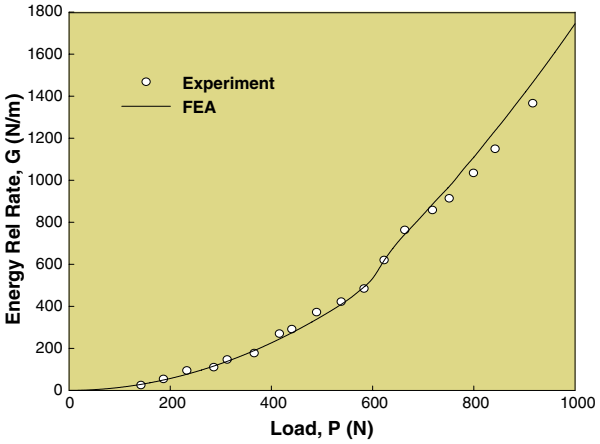

Fig. 4. Variation of energy release rate with load for crack–inclusion specimen and comparison with FEA.

A plot of G as a function of the applied load is plotted in Fig. 4 as a solid line. The energy release rate varies as a parabolic function relative to the applied load until the onset of debonding. When debonding occurs, a noticeable kink in the curve is evident.

4. Experimental validation

To validate numerical simulations, a specimen made of epoxy with a glass inclusion was prepared. Pyrex glass rods of diameter 3.8 mm, treated with silane to enhance bond strength with epoxy, were cut into cylinders of length 7.1 mm. The glass cylinder was then placed in a mold having a cavity thickness same as the length of the cylinder in such a way that its axis is perpendicular to the major dimensions of the mold. Two part epoxy[3] was then poured into the mold around the inclusion and cured at room temperature for 72 h. The cured samples were machined to the required dimensions. Subsequently, line gratings were printed on the specimen surface and the associated details are avoided here for brevity and can be found in Ref. [19]. The thickness of the 'interfacial bond layer' was found to be ~30 μm for an inclusion of diameter 3.8 mm as estimated from a microscopic measurement of a fabricated sample with silane coated glass cylinder. A notch was then cut into the edge of the specimen using a circular saw (thickness ~300 μm) and the notch tip was sharpened using a razor blade. Fig. 1b depicts the specimen geometry, dimensions and loading configuration with an illustration of grating direction. Here, L is the distance between the crack tip and the center of the inclusion of diameter d. Thus d/L ratio is a measure of the angle inclusion subtends at the crack tip and it was ~0.8 in the experimental work.

A moiré interferometer, schematically shown in Fig. 5, was developed to map surface displacements in the crack tip and inclusion vicinities as the sample was loaded monotonically. Two collimated He–Ne laser beams (wavelength 633 nm), originating from a single laser source, were used to create a virtual grating (standing wave) pattern over the physical grating (specimen grating) of density 200 lines per mm printed on the specimen, as shown. This choice of grating density provides a displacement sensitivity of approximately 0.4 fringes/μm. The resulting fringes due to interference between the virtual and physical gratings are governed by

$$v = N\frac{p_g}{2}, \quad N = 0, \pm 1, \pm 2, \ldots, \tag{6}$$

where v is the crack opening displacement at a generic point in the field, p_g is the pitch of the grating printed on the specimen (=5.08 μm in this work) and N is the fringe order of the light fringes [21].

Prior to loading, the specimen was placed in a displacement controlled loading device and a null field was obtained under no-load conditions by a careful alignment of optics. A digital camera was interfaced with a

[3] Epoxy used in this work was Epo-Thin™ (Product # 20-1840, 1842, 100 parts resin: 39 parts hardner) from Beuhler Inc., PA.

Please cite this article in press as: Savalia PC et al., A numerical study of inclusion–matrix debonding in the ..., Eng Fract Mech (2007), doi:10.1016/j.engfracmech.2007.05.012

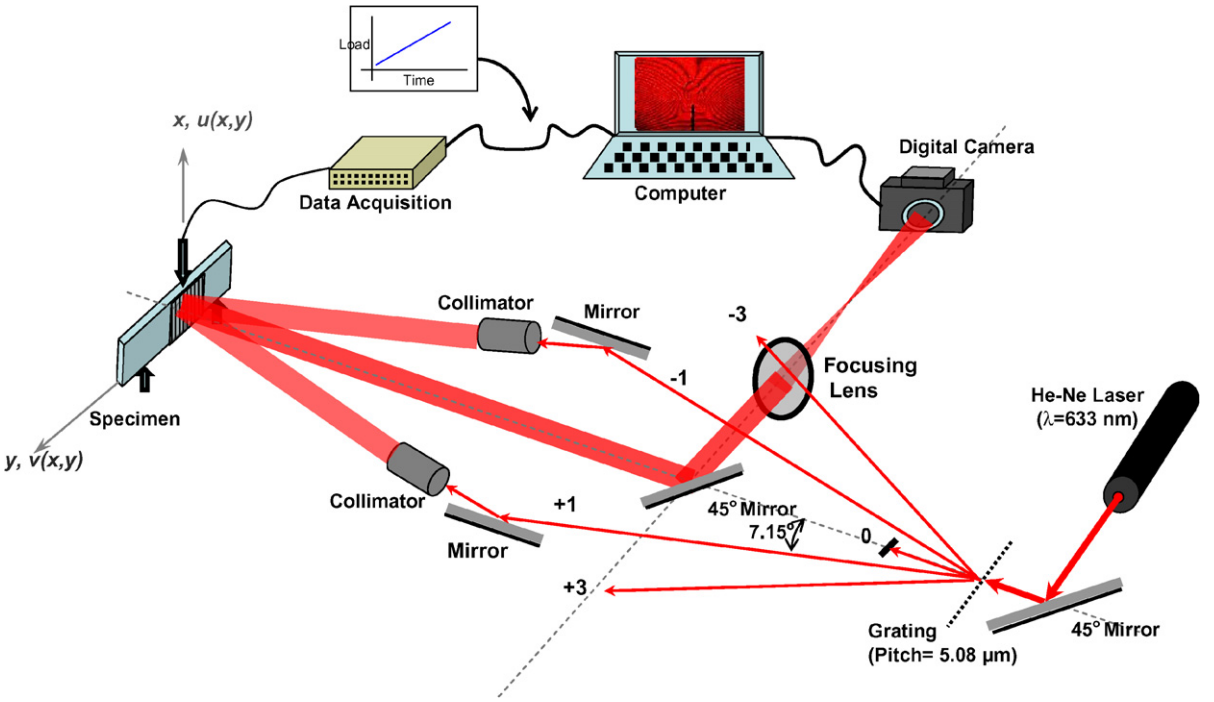

Fig. 5. Schematic of the moiré interferometer used to measure crack opening displacements near the crack–inclusion pair.

computer and was set to time-lapse photography mode to record interferograms at 2 s intervals during the loading phase. A load transducer, connected to a data logger, was used to record the load history at a rate of 5 samples/s during the event. The specimen was loaded quasi-statically in a three-point bend configuration at a cross-head speed of ~0.04 mm/s. The crack opening displacements (displacements perpendicular to the grating lines) were recorded as interference fringes. Four selected fringe patterns at different load levels are shown in Fig. 6. The first two interferograms are for load levels before the inclusion debonds from the matrix and the last two are after debonding occurs. The interferograms are nearly symmetric around the crack tip and suggest a dominant mode-I condition. However, fringes become discontinuous around the inclusion when debonding sets in. In the post-debonding regime, parallel and equally spaced fringes are also observed within the inclusion indicating rigid rotation of the inclusion due to an incomplete debonding between the inclusion and the surrounding matrix. Also, it should be noted that fringes around the inclusion become asymmetric after debonding, due to preferential debonding around the inclusion resulting from local inhomogeneities and unavoidable experimental asymmetries.

From the interferograms, CMOD values were calculated by counting the number of fringes around the crack up to the edge of the specimen. The data are shown in Fig. 3a as discrete symbols. A noticeable jump in CMOD when the inclusion debonds from the matrix is readily evident. These are similar to the results obtained from the numerical model. A related quantity namely the crack mouth compliance defined as $d(CMOD)/dP$, which brings out the evolution of debonding in a pronounced fashion, is shown in Fig. 3b. As seen in the simulations, once debonding occurs, compliance shows a substantial jump. In these plots, the data from the finite element model are also shown. A very good agreement between the two CMOD histories is evident in Fig. 3a. In Fig. 3b, a sudden increase in compliance following the onset of debonding is also evident. Further, a relatively higher plateau in compliance values in the post-debonding regime is attained when compared to the ones from the pre-debonding regime. The agreement between the optical measurements and the model provides a high degree of confidence in the numerical approach. The displacements along (r, $\theta = 180°$) were extracted from different interferograms to determine mode-I stress intensity factor, K_I from each interferogram. The method of regression of crack opening displacements was used for evaluating the values of K_I from each interferogram. More details can be found in Ref. [19].

Please cite this article in press as: Savalia PC et al., A numerical study of inclusion–matrix debonding in the ..., Eng Fract Mech (2007), doi:10.1016/j.engfracmech.2007.05.012

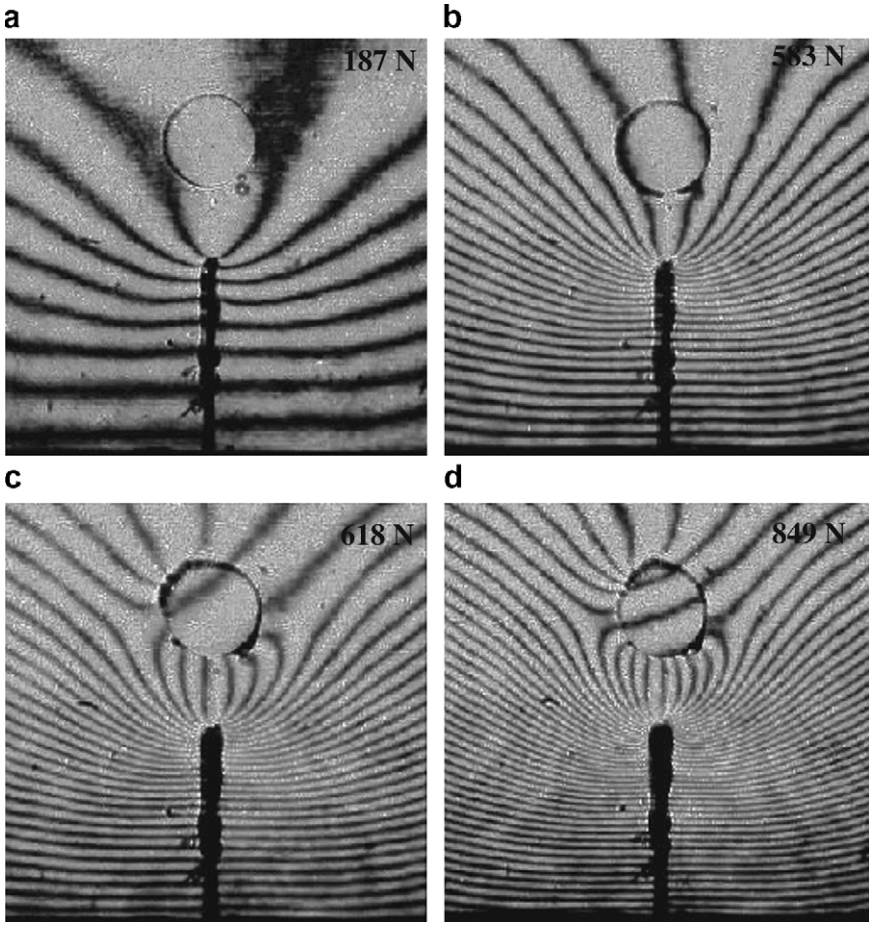

Fig. 6. Selected moiré interferograms for crack–inclusion specimen showing debonding between inclusion and matrix: (a), (b) before debonding and (c), (d) after debonding.

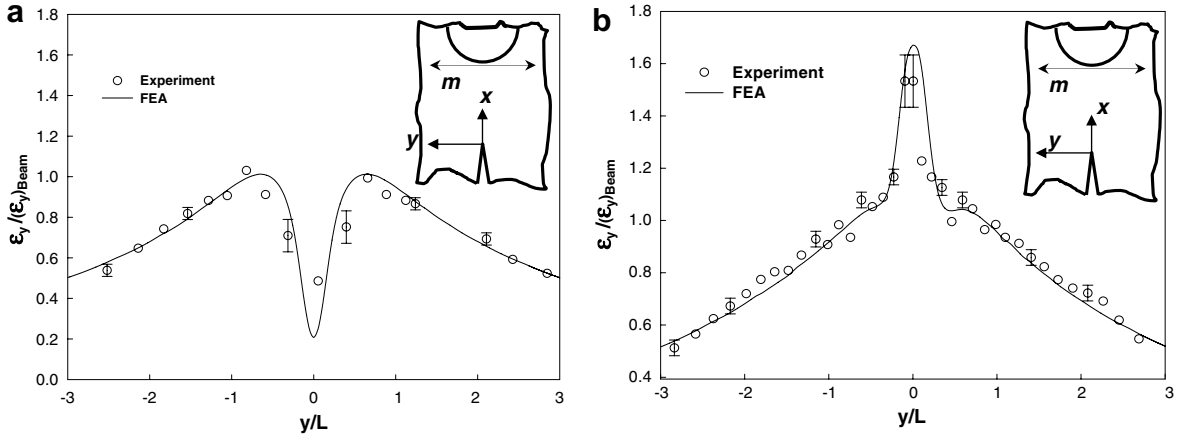

Fig. 7. Strain field evolution along ($x \sim 3$ mm, y) (shown by line 'm') for (a) pre-debonding and (b) post-debonding stages.

Next, the normal strain ε_y along a line ($x/L \sim 0.6$, y/L) (shown by a line marked 'm' in Fig. 7) near the inclusion–matrix interface obtained from the finite element model are presented. The strains in this plot are normalized by the maximum Euler-Bernoulli beam strains

Please cite this article in press as: Savalia PC et al., A numerical study of inclusion–matrix debonding in the ..., Eng Fract Mech (2007), doi:10.1016/j.engfracmech.2007.05.012

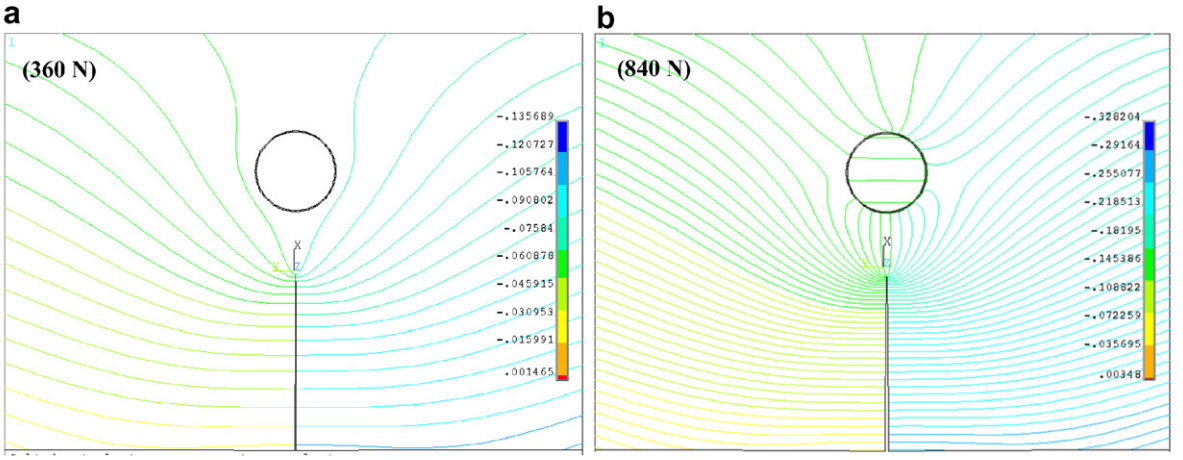

Fig. 8. Crack opening displacement field obtained from finite element analysis showing displacement contours in the crack–inclusion vicinity. (a) Before debonding and (b) after debonding. Contours levels are approximately same as the experimental ones. ($a = 8.5$ mm, $d = 4$ mm, $d/L \sim 0.8$, $E_i/E_m = 20$.)

$$(\varepsilon_y)_{\text{beam}} = \frac{3PS}{2EBW^2}, \tag{7}$$

where P and E denote the applied load and Young's modulus while others are geometric parameters of the beam shown in Fig. 1b. The plots are shown for pre- and post-debonding regimes in Fig. 7a and b, respectively. The experimental data is also shown on the same plot for comparison. The strain values from computations are in good agreement with the ones from the experiment. The larger differences between the two near the inclusion–matrix interface are not completely unexpected considering the asymmetries entering the model (see Fig. 1a) once the inclusion debonds from the matrix. The strain differences are also attributed to digitization and differentiation errors. Further, the fringe spacing in front of the crack was observed to decrease in the interferograms after debonding, which is reflected in the strain plot (Fig. 7b) as a steep increase.

After debonding occurs, a qualitatively similar progression of the debond front, as seen in experiments, was observed in the simulations. Representative plots of crack opening displacement fields from computations in the vicinity of the crack–inclusion pair, before and after debonding, are shown in Fig. 8. Here the contour levels are equal to the ones in the interferograms. A qualitative agreement between the optically recorded opening displacements (Fig. 6b and d) and the ones from the finite element analysis are also readily evident. Discontinuous fringes around the inclusion periphery seen in the interferograms (Fig. 6) can be observed in the numerical contour plots as well. Thus the overall crack tip behavior in terms of crack opening displacements is preserved in these simulations.

A user-defined macro was subsequently developed to extract mode-I stress intensity factors (K_I) from the finite element model. The linear regression of the crack opening displacements along $\theta = \pm\pi$ was used for the purpose and subsequently the energy release rates were calculated using Eq. (5). Again, a good agreement, including the distinct kink in G values at the onset of debonding, can be seen between experimental and numerical results plotted in Fig. 4.

5. Constant *d*/*L* ratio: effect of inclusion proximity

Next, a series of parametric studies were carried out using this numerical model. In the simulations, debonding of a glass inclusion from the epoxy matrix based on the criterion $\sigma_{rr} = (\sigma_{int})_{cr} = 9.2$ MPa was considered. The effect of inclusion proximity was studied for a constant d/L ratio. This ratio represents a constant angle subtended by the inclusion at the crack tip for different values of d and L. The model parameters used in these simulations are listed in Table 2.

Please cite this article in press as: Savalia PC et al., A numerical study of inclusion–matrix debonding in the ..., Eng Fract Mech (2007), doi:10.1016/j.engfracmech.2007.05.012

Table 2
Geometric parameters for constant d/L ratio of ~0.8 and $E_i/E_m = 20$, crack length (a) = 8.5 mm

	L (mm)	d (mm)	$\rho = \frac{(2L-d)}{2a}$	d/a
1	0.66	0.5	0.05	0.06
2	1.31	1.0	0.1	0.12
3	2.62	2.0	0.2	0.24
4	5.00	3.8	0.4	0.45
5	6.55	5.0	0.5	0.59
6	7.86	6.0	0.6	0.71
7	9.17	7.0	0.7	0.82
8	10.48	8.0	0.8	0.94

The variation of CMOD with the applied load is plotted in Fig. 9a for a constant d/L ratio of ~0.8. The inclusion proximity to the crack tip is identified by a nondimensional factor $\rho = \frac{2L-d}{2a}$ where a denotes the crack length. Physically, ρ represents the proximity of the crack tip to the inclusion–matrix interface. The applied load in these plots is normalized by P_0, the load at which a neat epoxy beam without any inclusion would fail in tension based on the ultimate strength of epoxy (σ_0). The value of P_0 was calculated as $P_0 = \frac{2\sigma_0 BW^2}{3S}$ where B is the thickness, W is the height of the beam and S is the span. (The failure load P_0 of an uncracked neat epoxy beam in this instance was based on a σ_0 value of 63 MPa for neat epoxy [19]). The individual graphs are clustered close to each other but show that debonding occurred at much higher loads for inclusions situated farther away from the crack tip. In order to further discern the effect of different values of L and d used in these simulations, the crack mouth compliance (d(CMOD)/dP) plots are shown in Fig. 9b. Each graph shows two distinct plateaus, one for pre- and the second for post-debonding states. (In this context it should be noted that the crack mouth compliance for a cracked neat epoxy beam without any inclusion was ~0.21 μm/N and details are not shown for brevity.) Further, at the onset of debonding, compliance in each case shows a jump followed by the attainment of a distinctly different maximum value reached in the post-debonding regime. When the inclusion is farther away from the crack tip, the pre-debond compliance values are lower while they become higher once debonding occurs.

The significance of crack mouth compliance can be inferred by examining energy release rates (G) in these cases. The values of G were calculated as described earlier and the corresponding plots, normalized by the ones for a neat epoxy beam without any inclusion, are shown in Fig. 10a. In these plots, each case has a distinct lower and an upper plateau for G. The jump in the value (ΔG) of energy release rate, before and after debonding, is an indicator of the severity of debonding on the crack tip behavior. The ΔG values, as a percentage

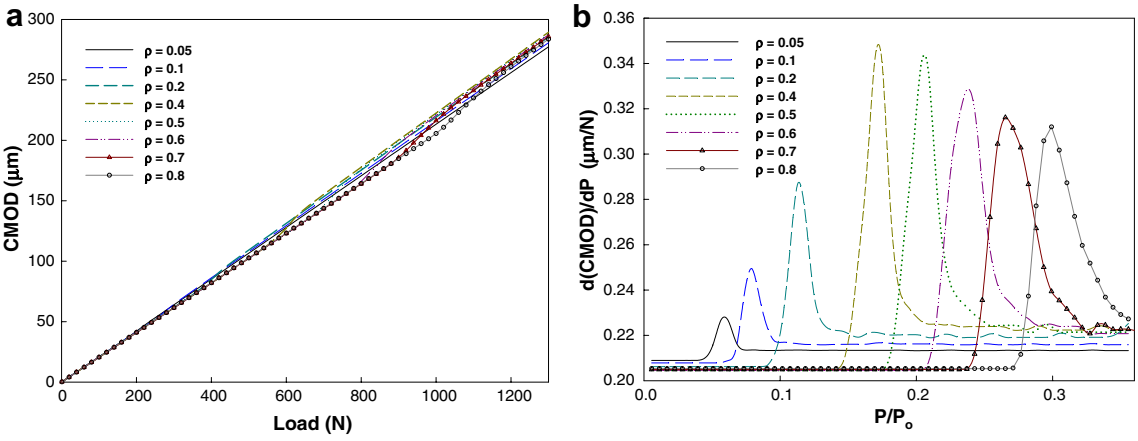

Fig. 9. Variation of (a) crack mouth opening displacement and (b) crack mouth compliance with applied load for different inclusion proximity parameter $\rho = (2L - d)/2a$. ($d/L \sim 0.8$, $E_i/E_m = 20$, $a = 8.5$ mm.)

Please cite this article in press as: Savalia PC et al., A numerical study of inclusion–matrix debonding in the ..., Eng Fract Mech (2007), doi:10.1016/j.engfracmech.2007.05.012

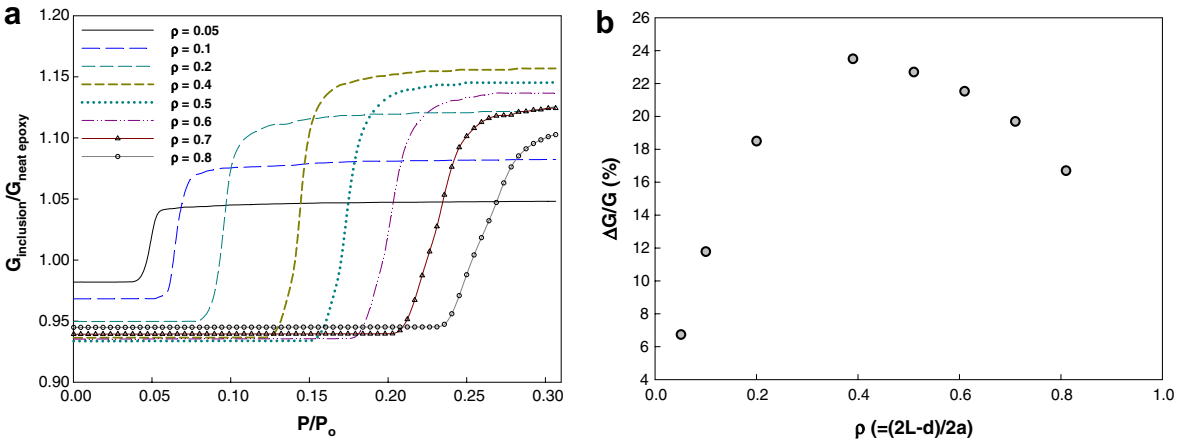

Fig. 10. Variation of (a) normalized energy release rate with normalized applied load and (b) percentage increase in crack driving force when inclusion debonds from the surrounding matrix, for different proximity parameter ρ. ($d/L \sim 0.8$, $E_i/E_m = 20$, $a = 8.5$ mm.)

relative to the corresponding value in the pre-debonding state, of each case are plotted in Fig. 10b as a function of the proximity parameter ρ. Evidently, ΔG increases monotonically for small inclusions until it reaches a peak value around $\rho \sim 0.4$ beyond which a continuous drop is seen suggesting $\rho \sim 0.4$ to be the least favorable configuration in terms of the fracture behavior when this inclusion debonds from the matrix.

The crack opening strains (ε_y) were also extracted from these simulations. Figs. 11a and b show plots of normalized ε_y along a line 'm' (see inset) parallel to the y-axis and nearly tangential to the inclusion in the pre- and post-debonding regimes, respectively. A normalized load of $P/P_0 = 0.023$ is considered for plots in Fig. 11a which corresponds to a load level well before debonding. For the post-debonding regime, $P/P_0 = 0.30$ which corresponds to a load level after debonding, is considered in Fig. 11b. In the pre- and post-debonding stages, an inclusion close to the crack tip experiences relatively steep strain gradients compared to the ones farther away. Prior to debonding (Fig. 11a), strains near the inclusion and ahead of the crack tip (in the vicinity of $y = 0$) are the lowest in all cases. The location of the highest strain moves away from the crack tip as ρ increases. Once the inclusion debonds (Fig. 11b), the trends are entirely reversed in the inclusion vicinity. The location of the highest strain concentration in the pre-debond situation changes from $y \neq 0$ to $y = 0$ after debonding. Also, after debonding, the inclusion closest to the crack tip shows the highest strain concentration compared to the ones that are farther away. In spite of this apparent monotonic behavior (relative to d/L), the ΔG variation as a function of proximity ρ is interestingly non-monotonic suggesting a complex interplay between the crack tip and inclusion fields.

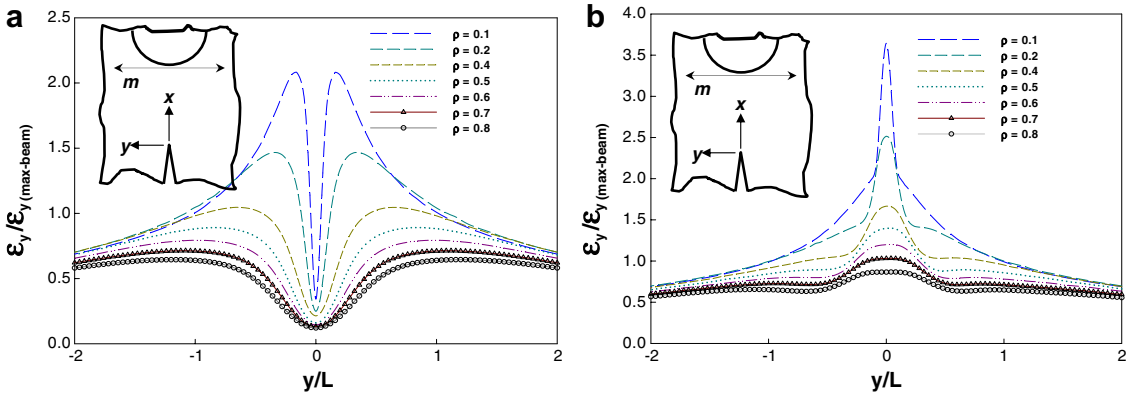

Fig. 11. Strain field evolution along line 'm' for (a) pre-debonding and (b) post-debonding regimes for different values of inclusion proximity parameter ρ. ($d/L \sim 0.8$, $E_i/E_m = 20$, $a = 8.5$ mm.)

Please cite this article in press as: Savalia PC et al., A numerical study of inclusion–matrix debonding in the ..., Eng Fract Mech (2007), doi:10.1016/j.engfracmech.2007.05.012

6. Varying d/L ratio: effect of inclusion size

Next, the d/L ratio was varied to examine the effect of the inclusion size on the crack tip behavior. In this case, the inclusion diameter (d) was varied whereas the distance between the crack tip and inclusion center L was kept constant. Thereby the angle subtended by the inclusion at the crack tip increases as d increases. The values of parameters L and d used in these simulations are tabulated in Table 3. As before, the elastic properties of the inclusion and matrix were those of glass and epoxy. The interfacial strength was also kept the same as the one used for constant d/L ratio simulations.

The evolution of CMOD as a function of the applied load for different cases is shown in Fig. 12a. Unlike in the previous simulations (Fig. 9a), CMOD plots visibly depart from each other once debonding occurs. Furthermore, it can be seen from the plots that as the d/L ratio increases (or as the inclusion size increases), the inclusion debonds at lower loads. Also, CMOD values are lower for higher d/L (due to greater crack tip shielding) before debonding whereas once it occurs the trend is entirely reversed. Further, noticeably higher slopes are associated with larger d/L ratios after the inclusion debonds. These are clearly evident in the crack mouth compliance plots shown in Fig. 12b. The (d(CMOD)/dP) values before and after debonding show opposite trends. Each graph shows a constant value of compliance (plateau) before debonding and is followed by a steep increase before retreating to a second but a higher value of constant compliance in the post-debond regime. Moreover, the jump in the compliance values increase as d/L ratio increases. Such an increasing trend in the compliance jump is reflective of the fact that when a large inclusion debonds, a greater loss of crack tip shielding (and reinforcement) occurs and the crack tip consequently experiences a higher driving force.

The normalized energy release rates were also computed and the resulting variation as a function of the applied load is shown in Fig. 13a. The observed trends are consistent with crack mouth compliance variations described above. In each case, the shielding effect on the crack tip exists before the occurrence of debonding.

Table 3
Geometric parameters used for studying inclusion size effect with elastic mismatch ratio $E_i/E_m = 20$

	L (mm)	d (mm)	d/a	d/L
1	5.0	1.0	0.12	0.2
2	5.0	2.0	0.24	0.4
3	5.0	3.8	0.45	0.8
4	5.0	5.0	0.59	1.0
5	5.0	6.0	0.71	1.2
6	5.0	7.0	0.82	1.4
7	5.0	8.0	0.94	1.6

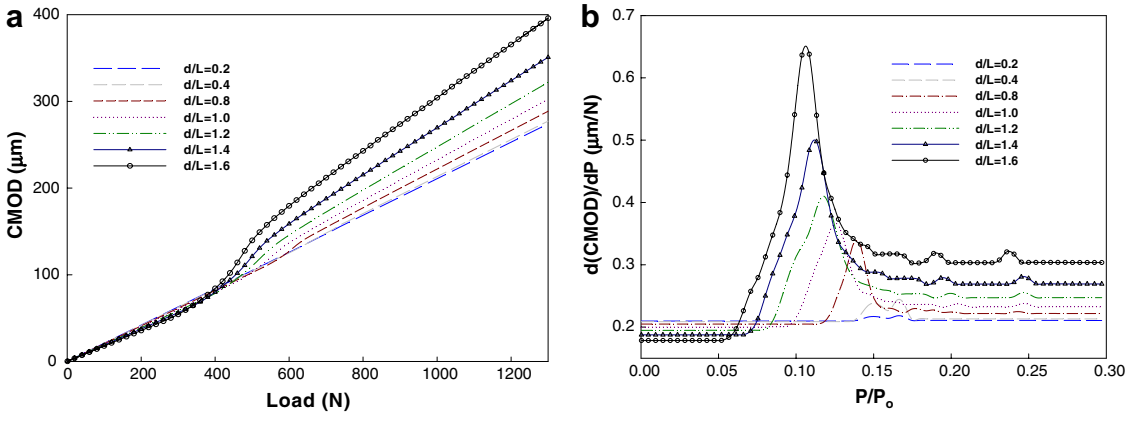

Fig. 12. Variation of (a) crack mouth opening displacement and (b) crack mouth compliance with applied load for different inclusion size parameter d/L. ($E_i/E_m = 20$, $a = 8.5$ mm, $L = 5$ mm.)

Please cite this article in press as: Savalia PC et al., A numerical study of inclusion–matrix debonding in the ..., Eng Fract Mech (2007), doi:10.1016/j.engfracmech.2007.05.012

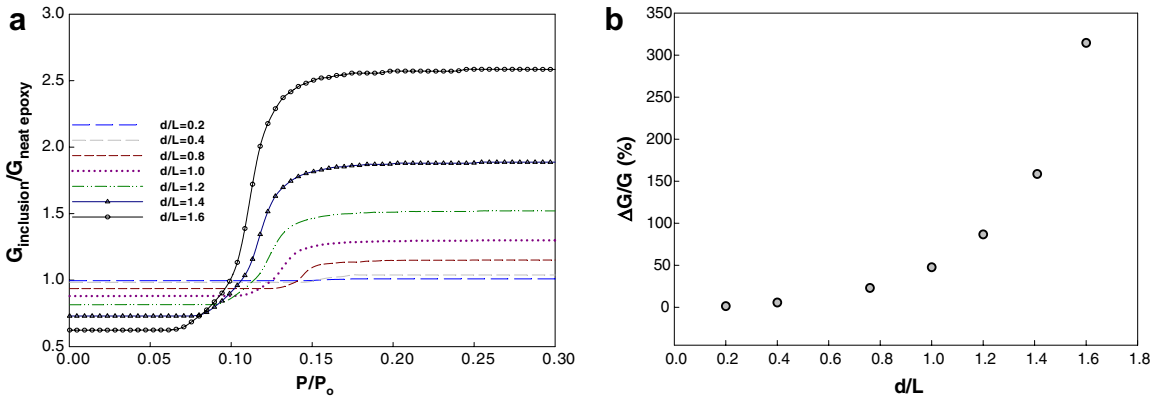

Fig. 13. Variation of (a) normalized energy release rate with normalized applied load and (b) percentage increase in crack driving force when inclusion debonds from the surrounding matrix, for different inclusion size parameter d/L. ($E_i/E_m = 20$, $a = 8.5$ mm, $L = 5$ mm.)

As the d/L ratio increases, debonding results in an increase in the energy release rate which stabilizes at a higher value. This behavior is highly pronounced at higher d/L ratios. For example, compared to the $d/L = 0.2$ with that for $d/L = 1.6$ the energy release rate is increased by approximately 2.5 times. A plot of this increase in the energy release rate as a function of d/L for all the cases considered is shown in Fig. 13b. The results suggest that for d/L ratios below ~0.4, the percentage increase in $\Delta G/G$ is rather small. The $\Delta G/G$ values, however, are dramatically higher at larger d/L ratios suggesting very high crack driving forces on the crack tip if a larger (and a stiff) inclusion debonds near a crack tip.

The crack opening strains (ε_y) were extracted and a few selected plots of strains along the line 'm' are shown in Fig. 14a and b. The corresponding load levels for each of these plots are kept the same as in Fig. 11a and b, respectively. Before debonding occurs, ε_y values increase as the line of symmetry ($y = 0$) is approached from the far field. The values of ε_y attain a maximum on both sides of the crack line but are a minimum in each case along the crack line. Higher strains are reached for larger inclusions. Once the inclusion debonds, ε_y values ahead of the crack dramatically increase with a characteristic dual hump variation. Again, strain values are much higher for larger inclusions and are consistent with the higher $\Delta G/G$ values observed in Fig. 13b for larger inclusions.

7. Varying E_i/E_m ratio: effect of Young's modulus mismatch

Next, the influence of elastic mismatch between the inclusion and the matrix was studied by varying the Young's modulus (E) of the inclusion relative to that of the matrix while keeping the interfacial debond

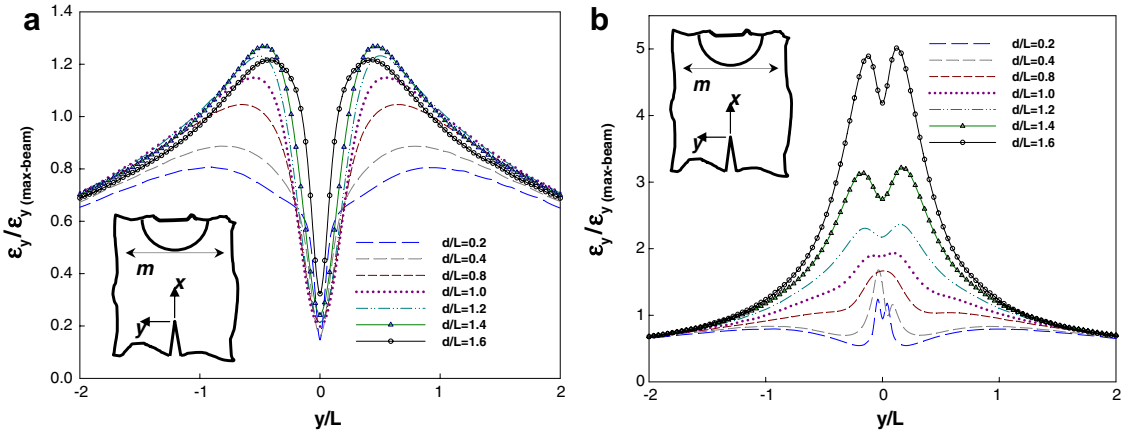

Fig. 14. Strain field evolution along line 'm' for (a) pre-debonding and (b) post-debonding regimes for different values of inclusion size parameter d/L. ($E_i/E_m = 20$, $a = 8.5$ mm, $L = 5$ mm.)

Please cite this article in press as: Savalia PC et al., A numerical study of inclusion–matrix debonding in the ..., Eng Fract Mech (2007), doi:10.1016/j.engfracmech.2007.05.012

strength same (9.2 MPa). The modulus ratio E_i/E_m, with subscripts i and m denoting the inclusion and the matrix, respectively, is varied from 20 to 0.2 with the former value being representative of the glass–epoxy combination. Also, in each of these simulations, the ratio d/L was kept constant at ~0.8 and d/a at ~0.45 with $d = 3.8$ mm, $L = 5$ mm. It should be noted that, the Young's modulus ratio $E_i/E_m = 1$ is also included for completeness and it implies a circular inclusion (or a plug) of Young's modulus same as that of the matrix but with a weak interface. In Fig. 15a, the crack mouth opening and crack mouth compliance results are presented. As in the earlier cases, CMOD values increase linearly with the applied load prior to the onset of debonding for all Young's modulus ratios. Each case shows a small yet noticeably different slope since the degree of crack tip reinforcement by inclusions of different moduli is different. Since the inclusion location and size in each case is the same, the graphs are clustered together over the entire load history. Yet, a visible kink in the linearity of each case marks the occurrence of debonding, delineating the pre- and post-debonding regimes. After debonding, graphs essentially follow parallel paths since d/L and d/a ratios are held constant in these simulations. The crack mouth compliance plots again bring out these subtle differences in a pronounced fashion in Fig. 15b. In each case the compliance value is constant until the onset of debonding. Each Young's modulus ratio produces a different initial constant level with stiffer inclusions producing smaller crack mouth compliances. In these plots debonding is punctuated by a spike in compliance followed by a drop to different but nearly identical value in the post-debonding regime. An inclusion debonds from the matrix at the lowest applied load for the stiffest inclusion and *vice-versa*. As the modulus ratio decreases, the load level at which debonding occurs shifts to a higher level monotonically.

The influence of inclusion debonding on the crack driving force (G) is captured in Fig. 16a. The normalized energy release rates (relative to that of a neat epoxy sample) are lower for stiffer inclusions when compared to the softer ones before the inclusion debonds. (As expected, the normalized G values are close to unity before the inclusion debonds for $E_i/E_m = 1$.) Once debonding occurs, the variation of G with load shows a jump, occurring at lower loads for stiffer inclusions when compared to the softer ones. Furthermore, the normalized G values attain nearly the same value upon the completion of debonding process since the inclusion size and its proximity to the crack tip are held constant during the simulations. In Fig. 16b, the relative jump in the crack driving force $\Delta G/G$ due to debonding at a constant interfacial strength is quantified as a percentage. A monotonic increase in the $\Delta G/G$ values as a function of the modulus ratio is evident. The effect of the modulus ratio is most pronounced in the range 0.2–1.0 with a ~20% jump in $\Delta G/G$. The effect, however, saturates quickly when the modulus ratio is further increased.

The variations of normalized crack opening strains along a line 'm' (see, insets in Fig. 14) ahead of the crack and nearly tangential to the inclusion are shown in Fig. 17a and b. The plots in Fig. 17a correspond to different pre-debond scenarios. Prominent differences in strain variations seem to be limited to the range $-0.3 < y/L < 0.3$, showing a highly localized phenomena. The normalized strains directly ahead of the crack

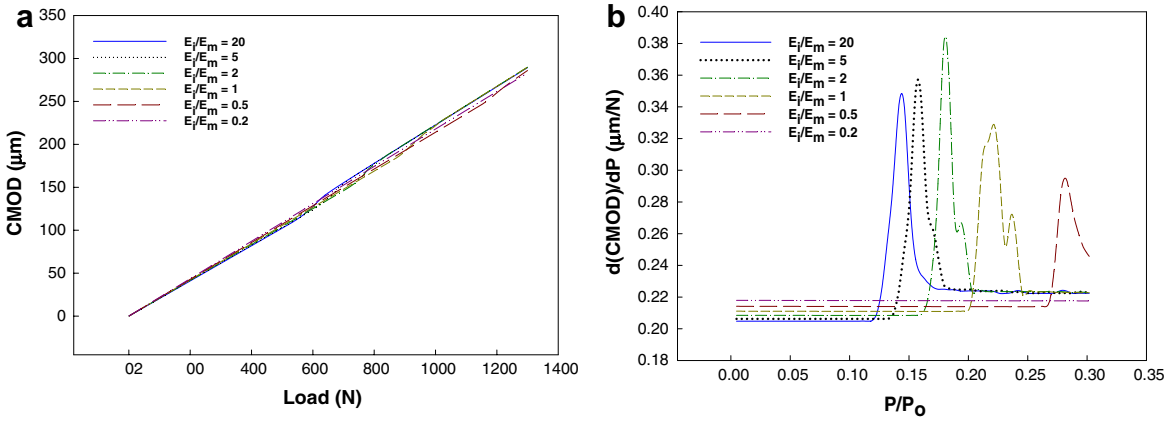

Fig. 15. Variation of (a) crack mouth opening displacement and (b) crack mouth compliance with applied load for different Young's modulus ratios. ($d/L \sim 0.8$, $d/a \sim 0.45$ with $d = 3.8$ mm.)

Please cite this article in press as: Savalia PC et al., A numerical study of inclusion–matrix debonding in the ..., Eng Fract Mech (2007), doi:10.1016/j.engfracmech.2007.05.012

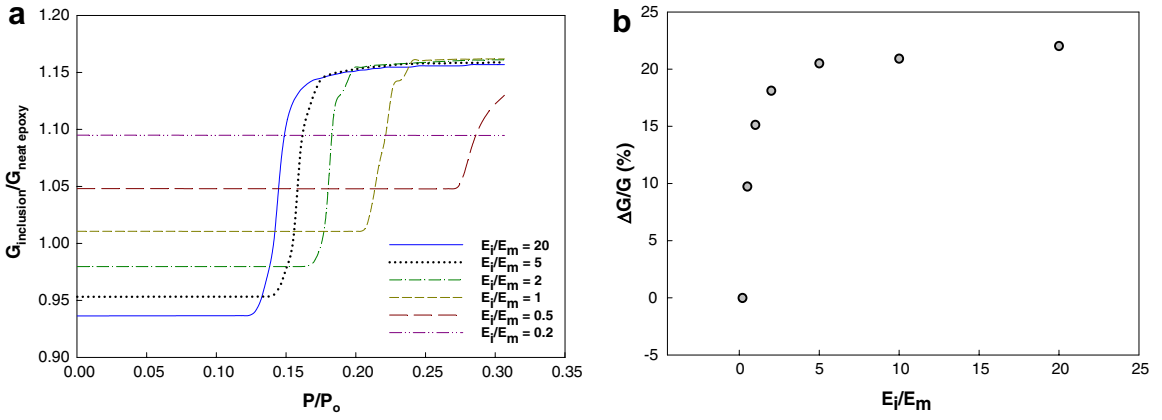

Fig. 16. Variation of (a) normalized energy release rate with normalized applied load and (b) percentage increase in crack driving force when inclusion debonds from the surrounding matrix, for different inclusion to matrix Young's modulus ratios. ($d/L \sim 0.8$, $d/a \sim 0.45$ with $d = 3.8$ mm.)

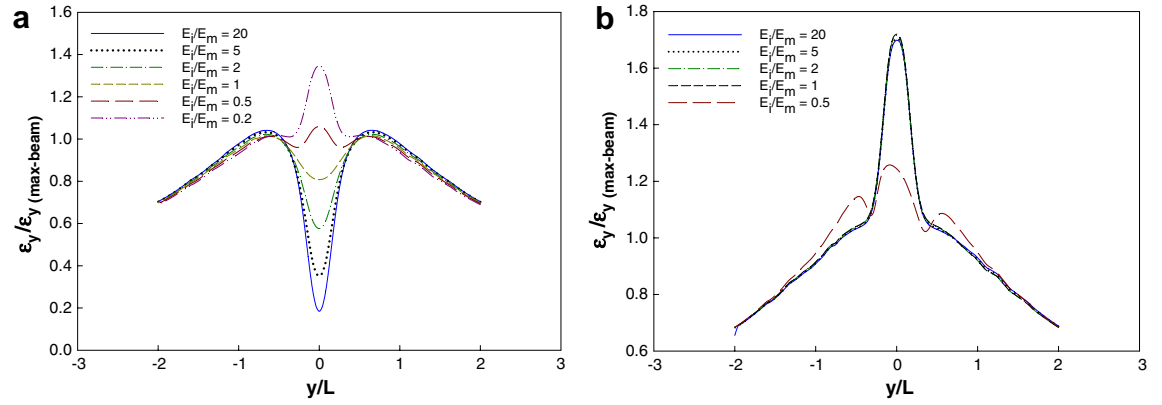

Fig. 17. Strain field evolution along line '*m*' (see inset in Fig. 14) for (a) pre-debonding and (b) post-debonding regimes for different values of inclusion to matrix Young moduli ratios. ($d/L \sim 0.8$, $d/a \sim 0.45$ with $d = 3.8$ mm.)

tip but close to the inclusion boundary progressively increase as inclusions become softer relative to the matrix. In cases of $E_i/E_m = 0.5$ and 0.2, the plots show minimum values not at ($x \approx L$, $y = 0$) but at a finite value of $|y|$ instead. A local maximum occurs at ($x = L$, $y = 0$) for this case. After debonding, the normalized strains along the same line show somewhat different distributions for stiffer and softer inclusion cases. In the former, the normalized strains spike to a rather high value of approximately 1.7 along ($x \approx L$, $y = 0$). In the latter case, however, debonding of the inclusion rises the strain levels at distances farther away from the crack line ($0.3 < |y/L| < 1$) with a much lower peak compared to the former. (It should be noted that strain plot for $E_i/E_m = 0.2$ is not included in Fig. 17b because debonding did not occur at the load levels used in the current simulations.) Such a redistribution of strains due to debonding suggests lower jump in the crack driving force when a softer inclusion debonds from the matrix relative to the stiffer ones.

8. Summary

Debonding of an inclusion from the surrounding matrix and the associated consequences on a nearby crack tip are studied numerically. Two-dimensional finite element models of symmetric three-point bend beam configuration, each with an edge crack and a cylindrical inclusion ahead of the crack tip, are developed. A stiffness

Please cite this article in press as: Savalia PC et al., A numerical study of inclusion–matrix debonding in the ..., Eng Fract Mech (2007), doi:10.1016/j.engfracmech.2007.05.012

degradation/deactivation method coupled with a tensile critical radial stress criterion is used to simulate the evolution of inclusion–matrix interfacial debonding process during monotonic loading. The approach is validated by comparing numerical results with the corresponding ones obtained from moiré interferometry experiments on a glass–epoxy material combination. Excellent agreement between the two for crack opening displacements, crack mouth compliance, crack driving forces, dominant strains at critical locations, all point to the viability of the methodology for such simulations.

The numerical model is extended to examine the effects of inclusion proximity, inclusion size, and the Young's modulus mismatch between the matrix and the inclusion on crack tip parameters. The following are some of the major observations of this work:

1. For a constant inclusion diameter to location ratio (d/L), the effects of inclusion–matrix interface proximity to the crack tip are studied for a fixed Young's modulus ratio of 20. If the inclusion interface is father away from the crack tip, pre-debond crack mouth compliance values decrease but the ones from the post-debond regime increase. Also, farther the inclusion interface is from the crack tip, higher load levels are necessary to debond the inclusion. A jump in the crack tip energy release rate indicates the impending severity of the debonding phenomenon. The highest percentage jump occurs when the proximity parameter (ρ) is approximately 0.4. A reduction in the amount of this jump is evident at lower as well as larger proximities relative to $\rho \sim 0.4$.
2. In the simulations involving different inclusion diameter to location ratios, the effects of inclusion size are studied again for a fixed Young's modulus ratio of 20. The results show that the relative jump in crack mouth compliance increases with the inclusion size, suggesting a greater loss of crack tip shielding upon debonding. Consequently, higher crack driving forces occur when a larger inclusion debonds from the surrounding matrix. The percentage increase in energy release rates are dramatically higher when d/L ratios exceed $\sim$0.4.
3. In the study of elastic mismatch between the inclusion and matrix, the proximity and size parameters are held constant at $\rho \sim 0.45$ and $d/L \sim 0.8$ while Young's modulus ratio (E_i/E_m) is varied from 0.2 to 20. The effects are most prominent when E_i/E_m varies from 0.2 to 1. The stiffer the inclusion, tendency to debond from the surrounding matrix at lower loads is greater when the interfacial strength is fixed at a constant value. And, the load at which debonding occurs increases monotonically as the inclusion becomes more compliant. In the pre-debond regime, a stiffer inclusion produces a lower crack driving force due to higher reinforcement. A rapid increase is also seen in the percentage jump in the crack driving force when E_i/E_m ratio changes from being <1 to >1.

Acknowledgement

A partial support for this research from a grant from National Science Foundation (NSF-CMS-0509060) is gratefully acknowledged.

References

[1] Tamate O. The effect of a circular inclusion on the stress around a line crack in a sheet under tension. Int J Fract Mech 1968;4:257–266.
[2] Atkinson C. The interaction between a crack and an inclusion. Int J Engng Sci 1972;10:127–36.
[3] Erdogan F, Gupta GD, Ratwani M. Interaction between a circular inclusion and an arbitrarily oriented crack. J App Mech 1974;41:1007–13.
[4] Gduotos EE. Interaction effects between a crack and a circular inclusion. Fibre Sci Technol 1981;15(1):27–40.
[5] Gduotos EE. Stable crack growth of a crack interacting with a circular inclusion. Theor Appl Fract Mech 1985;3(2):141–50.
[6] Hasebe N, Okumura M, Nakumura T. Stress-analysis of a debonding and a crack around a circular rigid inclusion. Int J Fract 1986;32(3):169–83.
[7] Patton EM, Santare MH. The effect of a rigid elliptical inclusion on a straight crack. Int J Fract 1990;46:71–9.
[8] Li R, Chudnovsky A. Energy analysis of crack interaction with an elastic inclusion. Int J Fract 1993;63:247–61.
[9] Li R, Chudnovsky A. The stress intensity factor Green's function for a crack interacting with a circular inclusion. Int J Fract 1994;67:169–77.
[10] Bush M. The interaction between a crack and a particle cluster. Int J Fract 1997;88:215–32.

Please cite this article in press as: Savalia PC et al., A numerical study of inclusion–matrix debonding in the ..., Eng Fract Mech (2007), doi:10.1016/j.engfracmech.2007.05.012

[11] Knight MG, Wrobel LC, Henshall JL, De Lacerda LA. A study of the interaction between a propagating crack and an uncoated/coated elastic inclusion using BE technique. Int J Fract 2002;114:47–61.
[12] Kitey R, Phan AV, Tippur HV, Kaplan T. Modeling of crack growth through particulate clusters in brittle matrix by symmetric-Galerkin boundary element method. Int J Fract 2006;141(1):11–25.
[13] Xu XP, Needleman A. Numerical simulation of fast crack growth in brittle solids. J Mech Phys Solids 1994;42(9):1397–434.
[14] Xu XP, Needleman A. Numerical simulations of dynamic interfacial crack growth allowing for crack growth away form the bond line. Int J Fract 1995;74:253–75.
[15] Madhusudhana KS, Narsimhan R. Experimental and numerical investigations of mixed mode crack growth resistance of a ductile adhesive joint. Engng Fract Mech 2002;69:865–83.
[16] Al-Ostaz A, Jasiuk I. Crack initiation and propagation in materials with randomly distributed holes. Engng Fract Mech 1997;58(5–6):95–420.
[17] Ko D, Kim B, Choi J. Finite-element simulation of the shear process using the element-kill method. J Mater Process Tech 1997;72:129–40.
[18] ANSYS users's manual (Version 10). Cannonsburg, PA: ANSYS; 10, 2005.
[19] Savalia PC, Tippur HV. A study of crack–inclusion interaction using moiré interferometry and finite element analysis. Exp Mech, in press, doi:10.1007/s11340-006-9021-9.
[20] Rousseau C-E, Tippur HV. Influence of Elastic Gradient Profiles on Dynamically Loaded Functionally Graded Materials: Cracks Along the Gradient. Int J Solids Struct 2002;38:7839–56.
[21] Post D, Han B, Ifju P. High sensitivity moiré. New York: Springer-Verlag; 1994.

Please cite this article in press as: Savalia PC et al., A numerical study of inclusion–matrix debonding in the ..., Eng Fract Mech (2007), doi:10.1016/j.engfracmech.2007.05.012